Deep learning-guided joint attenuation and scatter correction without the use of anatomical imaging in multitracer neuroimaging

By Karin Bortolin

A thesis submitted to the Faculty of Medicine of the University of Geneva
in partial fulfillment of the requirements for the
Degree of Interdisciplinary Master of Neuroscience

Master Adviser:
Prof. Habib Zaidi

Jury:
Prof. Philippe Millet
Prof. Sylvain Sardy

Geneve, 22/12/2019

Faculty of Medicine

Interdisciplinary Center of Neuroscience

Abstract

The quantification of brain functional activity from PET images is based on the detection of photons as signal emitted by the brain. Therefore, the correction for photons that are not detected (attenuated) or detected at the wrong localization (scattered) is an essential requirement. For physical reasons, PET attenuation and scatter correction is challenging on systems lacking x-ray CT or transmission scanning, such as dedicated brain PET scanners and hybrid PET/MRI systems. In the literature, when CT or transmission information is missing, as is the case of hybrid PET/MRI, MR images are used to generate pseudo-CT images, while in the case of dedicated brain PET scanners, calculated attenuation correction when transmission scanning is lacking. This work focuses on the quantitative assessment of a novel method based on deep learning to generate PET images corrected for attenuation directly from the uncorrected PET images without using any anatomical imaging, such as CT and MRI. In this study, 160 patients underwent TOF PET/CT scans using one of the 4 different radiotracers (40 patients for each radiotracer), namely ^{18}F-FDG, ^{18}F-DOPA, ^{18}F-Flortaucipir,and ^{18}F-Flutemetamol. A deep convolutional neural network implemented in the NiftyNet platform was trained to generate corrected PET images from uncorrected PET images. The quantitative evaluation of this approach was conducted separately for each radiotracer considering the PET images corrected using CT information as reference. Moreover, corrected PET images using the 2-class segmentation method were included for evaluation. The latter is a segmentation-based attenuation and scatter correction method used on PET/MRI scanners in the clinic, providing a bottom-line for clinically relevant performance evaluation. Finally, special attention was given to the presence of large errors that may occur when using deep learning techniques. The quantitative analysis of PET images demonstrated superior performance of the deep learning method compared to the segmentation-based approach for all radiotracers. Despite the promising results, the deep learning methods are vulnerable to outliers, resulting in large errors in 6 of the 160 brain PET images. Therefore, caution is required when employing this approach in the clinic.

This thesis is based on work currently submitted for publication to the journal Medical Image Analysis.

Acknowledgements

I would like to thank Prof. Habib Zaidi for his guidance and presence. His door office was always open whenever I had a question.

Thanks to Dr. Hossein Arabi for his patience and for sharing expertise. I am grateful to his valuable and constructive suggestions.

I would like to thank Dr. Nathalie Ginovart, Dr. Valentina Garibotto and Dr. Alessandra Dodich for their help with the clinical studies and the tracer-specific templates.

A very special gratitude goes to people in the PINLAB, who continuously encourage me. It was great sharing laboratory with them during the last year.

I am also grateful to my family and friends who gave me moral and emotional support along the way.

Contents

List of Abbreviations

2D	2-dimensional
3D	3-dimensional
AC	Attenuation correction
CTAC	Computed tomography attenuation correction
DLAC	Deep learning attenuation correction
FWHM	Full width at half maximum
HU	Hounsfield unit
kVp	Kilovolt peak
LOR	Line of response
MAE	Mean absolute error
mAs	Milliampere-seconds
ME	Mean error
mm	Millimiter
MRI	Magnetic resonance imaging
nonAC	None attenuation correction
PET	Positron emission tomography
RE	Relative error
ReLU	Rectified linear unit
RMSE	Root mean squared error
sec	Second
SegAC	Segmentation attenuation correction
SUV	Standard uptake value
TOF	Time-of-flight
PSNR	Signal-to-noise ratio
SSIM	Structural similarity index

List of Figures

List of Tables

Chapter 1

Introduction

1.1 Positron Emission Tomography

Positron emission tomography (PET) is a molecular imaging technique that uses radioactive compounds to enable the in vivo visualization of a variety of physiologic and chemical processes in the body. It can be used in imaging studies of humans as well as of animals (Wernick and Aarsvold, 2004). In principle, a positron-emitting radiopharmaceutical (also called radiotracer) is injected into the vein of the patient prior to PET acquisition. Subsequently, the patient is positioned in a machine, called PET scanner, having a large tunnel at its center. Pairs of annihilation photons emitted indirectly by the radiotracer following positron-electron annihilation are eventually detected by the ring of detectors forming the PET scanner.

PET is a non-invasive imaging modality currently playing a key role in a wide range of clinical and research applications. In clinical setting, it is used to evaluate the function of organs, such as the brain or heart, or to detect cancer and assess the effectiveness of a treatment plan (Bailey et al., 2005). In fact, in many diseases, the biochemical activity of cells changes. For example, brain cells affected by dementia consume less energy than normal brain cells whereas heart cells deprived of adequate blood flow begin to die. Cancer cells, on the contrary, multiply at a faster rate, they are more active than normal cells and as such, the utilization of glucose is significantly enhanced. PET images enable the detection of the these cellular changes, providing a novel way for molecular diagnostics and molecular therapies. Its use has greatly enhanced our understanding of the pathophysiology of central nervous system diseases, such as schizophrenia, depression, Parkinson, Alzheimer, dementia, and epilepsy (Politis and Piccini, 2012). In oncology, it is used to detect many types of cancer, such as pulmonary, colorectal, breast, lymphoma, head, neck, bone, ovarian and GI cancers (Kubota, 2001).

1.2 Hybrid Imaging (PET/CT and PET/MRI)

PET scanning alone is not capable of providing accurate anatomical information to localize the metabolic abnormalities. Therefore, today all PET scanners are coupled to x-ray computed tomography (CT) or magnetic resonance imaging (MRI) systems and are referred to as PET/CT or PET/MRI systems, respectively. CT imaging and MR imaging provide static anatomical information enabling the identification of disease states on the basis of anatomical changes, while PET imaging provides information on the biochemical processes which may often be seen well before structural changes (Shim et al., 2005). In fact, when the cellular activity begins to be abnormal, also body tissue and structures can be affected. For example, cancer cells may form a mass or the loss of brain cells of some central nervous system diseases could result in overall brain volume or density decrease. Therefore these hybrid systems offer the synergy of capturing structural as well as physiological information in a one stop shopping exam, improving the localization of any accumulation of the radiotracer.

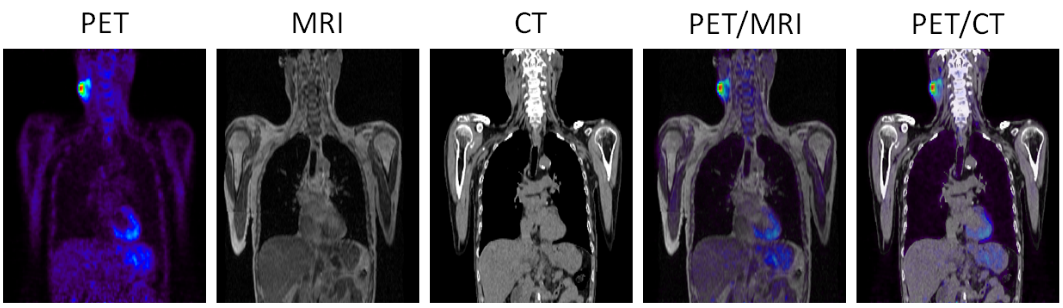

Figure 1.1: MR imaging provides high spatial resolution and excellent soft tissue contrast, while CT imaging provides excellent details about bony structures. PET imaging reveals radiotracer accumulation while the fusion of MRI and CT with PET captures structural as well as physiological information in one image.

1.3 Positron Emission Tomography radiotracers

The radiotracer used during PET scans provides the basis both for image quality and clinical indication. It consists of two parts: (1) a ligand that interacts with a specific target in the body and (2) a radioactive atom made of a positron-emitting radionuclide (Wadsak and Mitterhauser, 2010). This last component is produced in a particle accelerator called cyclotron to provide signal detectable by the PET scanner. Different types of radiotracers are designed to serve different purposes depending on the target site; for instance a receptor system, antigen, enzyme or transporter. In fact, radiotracers can be made to accumulate in cancerous tumors or regions of inflammation, or to bind to specific proteins in the brain like in the case of central nervous system diseases. In the following section, the radiotracers used in this study are briefly described.

1. ^{18}F-FDG is the most widely used radiotracer in clinical practice constituting a powerful imaging tool. Nowadays, it is used mainly in oncology, but ^{18}F-FDG PET imaging is also widely used in other clinical applications, such as Alzheimer's disease, dementia, epilepsy, brain trauma, Huntington disease, cerebrovascular disorders, brain tumors, schizophrenia, and mood disorders (Newberg, Alavi, and Reivich, 2002; Tai and Piccini, 2004). The use of ^{18}F-FDG in oncology is motivated by the fact that cancer cells increase the uptake of glucose or glucose-analogues as deoxy-glucose. This radiotracer is formed by labeling deoxy-glucose with the positron emitting radionuclide ^{18}F to enable cancer cells to be detectable by a PET scanner.
2. ^{18}F-DOPA is a radiotracer used to evaluate the activity of aromatic l-amino acid decarboxylase of the dopaminergic system. In fact, after being injected into the blood stream, it reaches the dopaminergic cells in the brain and is used as a precursor for dopamine. For this reason, ^{18}F-DOPA is suitable to investigate the presynaptic striatal dopaminergic function in neurologic disorders, such as Parkinson's disease or other neurodegenerative diseases with motor dysfunction (Shinotoh and Calne, 1995). Moreover it is also an excellent radiotracer to detect neuroendocrine tumors that are capable of accumulating and decarboxylate amine precursors (Pantaleo et al., 2008).

3. ^{18}F-Flutemetamol is a radiotracer intended for PET imaging of the brain because it binds to β-amyloid aggregates. Therefore it is used in elderly patients with cognitive impairment who are being evaluated for Alzheimer's disease and other causes of cognitive decline (Chiotis et al., 2017). In fact, a significant amount of amyloid neuritic plaque is present in patients with Alzheimer's disease and other types of neurologic conditions.
4. ^{18}F-Flortaucipir is another radiotracer used to estimate the β-amyloid neuritic plaque density in the brain of adult patients with cognitive impairments (Yang, Rieves, and Ganley, 2012).

1.4 Attenuation and scatter correction

PET imaging is based on the detection of annihilation photons by a number of detector rings surrounding the patient inside the scanner. Once the radiotracer is injected, it accumulates in the body's tissues and organs and its natural decay includes the emission of positrons that will make multiple collisions with nearby electrons. The collision, known as annihilation, produces energy in the form of a pair of annihilation photons that travel in nearly opposite directions as shown in Figure 1.2. The PET scanner records the coincident photons and a computer analyzes them to create a three-dimensional image enabling the visualization of the radiotracer distribution in the body. Not all the emitted photons are correctly detected because some of them

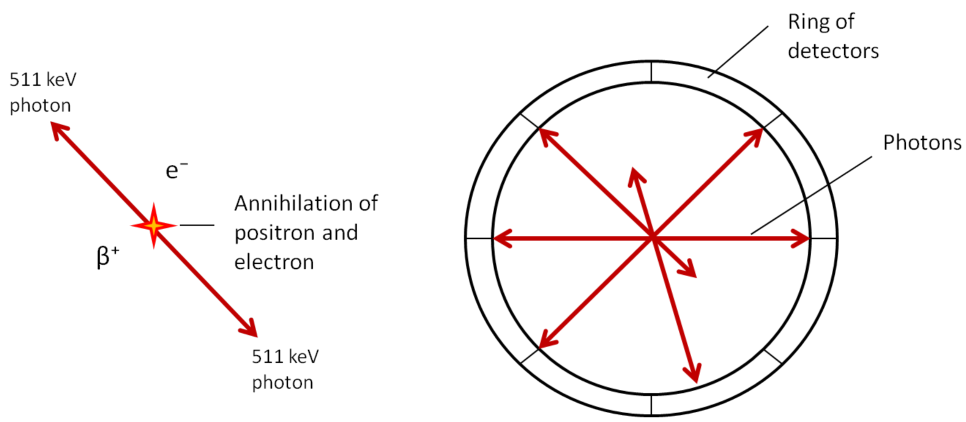

Figure 1.2: Annihilation coincidence detection. When a positron annihilates with an electron, two 511-keV photons are emitted in nearly opposite directions (left). When two photons are simultaneously detected by the crystals (right), it is presumed that an annihilation event occurred on the line connecting the photons, which is called a line of response (LOR).

are absorbed and mostly scattered in tissues, thus degrading the quality and accuracy of reconstructed PET images. This is due to Compton scattering, which is the most relevant interaction between 511-keV photons and matter inside the body. Photons that undergo Compton scattering will deviate from their original trajectory, loosing energy and resulting in photons not detected (attenuation) or detected at the wrong localization (scatter). Therefore, attenuation and scatter correction is an essential requirement to accurately quantify the radiotracer uptake (Zaidi, 2001).

The main challenge for attenuation and scatter correction of PET images is to find reliable attenuation correction factors, which are usually calculated from an attenuation map (Berker and Li, 2016). The attenuation map contains the linear attenuation coefficients which represent the probability of interaction between the photons and the matter in the body (Zaidi and Hasegawa, 2003) and it can also be used to correct for Compton scattering (Zaidi and Koral, 2004). For this purpose, CT images are ideal because they reflect the electron density and an attenuation map is derived using a linear transformation of CT values. Yet, delineation of anatomical details on CT images is challenging in some regions owing to low soft-tissue contrast, which hinders clinical diagnosis. On the other hand, MRI offers superior anatomical details, but the MRI signal do not directly provide attenuation information because they reflect proton densities and relaxation time properties of biological tissues, thus limiting the power of the PET/MRI systems. Therefore, PET scanners coupled to MRI require accurate and robust attenuation correction. Furthermore, over the years, the introduction of novel specific radiotracers triggered the development of dedicated brain PET systems that allow for significantly higher spatial resolution compared to conventional whole-body PET scanners (Zaidi and Montandon, 2006). These dedicated brain PET systems face also the substantial challenge of attenuation and scatter correction since they do are not always equipped to acquire anatomical images (Melroy et al., 2017, Tashima and Yamaya, 2016). To compensate for these deficiencies when CT is not available, different attenuation and scatter correction methods either with or without the use of structural MR images have been developed. These strategies can be mainly divided into the following four principal categories: segmentation methods, atlas-based approaches, machine learning techniques and emission-based methods (Mehranian, Arabi, and Zaidi, 2016b).

1. In segmentation methods, the derivation of the attenuation map is obtained categorizing the MR images into classes and assigning to each class a predefined tissue-specific attenuation coefficient. (Martinez-Möller et al., 2009a, Arabi et al., 2015). The classes consist mainly of soft tissues, adipose tissue, lungs, air cavities, and bones. The number of classes varies between the different method variants.
2. Atlas-based approaches rely on co-registered pairs of MR/CT images to generate substitute CT image. The derivation of the attenuation map is obtained from preacquired CT or transmission images (Montandon and Zaidi, 2005), that are then non-linearly warped to match the target patient's anatomy (Zaidi, Montandon, and Meikle, 2007).
3. Machine learning techniques aim to train a classifier, which segments MR images or to directly convert the intensities of the MR image into linear attenuation coefficients of the corresponding CT image.
4. Emission-based methods estimate the attenuation map only from PET emission data during PET image reconstruction using the maximum likelihood reconstruction of activity and attenuation (MLAA) algorithm (Benoit et al., 2016). With the advent of TOF PET/MRI scanners, this method took advantage of the availability of time-of-flight (TOF) information (Defrise, Rezaei, and Nuyts, 2012) to improve the signal-to-noise ratio (SNR) of reconstructed images.

Recently, owing to the impressive versatility of deep learning techniques, a new methodology for attenuation and scatter correction has been reported (Shiri et al., 2019,Yang et al., 2019). A deep convolutional neural network was trained to learn the conversion between non-attenuation and scatter corrected (PET-nonAC) and CT-based attenuation and scatter corrected PET (PET-CTAC) images in the image-space and without using the anatomical information. This approach has been evaluated only on brain 18F-FDG PET images. The aim of this work is to carry out an assessment of novel methods based on deep learning techniques to generate corrected PET images for attenuation and scatter directly from the uncorrected PET images without using any anatomical images for various PET neuroimaging radiotracers. The performance of the method has been investigated using 160 PET/CT brain scans using four different radiotracers (40 for each radiotracer), namely ^{18}F-FDG, ^{18}F-DOPA, ^{18}F-Flutemetamol, and ^{18}F-Flortaucipir. A deep convolutional neural network was trained considering PET-CTAC images as reference for evaluation. Moreover, a segmentation-based attenuation map (SegAC) derived from a 2-class (background air and soft-tissue) segmentation of PET-nonAC images was included in the evaluation as a proxy for segmentation-based attenuation and scatter correction used on PET/MRI scanners in the clinic (Zaidi et al., 2011). Particular attention was paid to images corrected using the deep learning method, searching for large errors which might occur when using these techniques.

Chapter 2

Materials and Methods

2.1 Data acquisition

In this study, 160 patients that underwent PET/CT time-of-flight (TOF) brain imaging were included. Current generation TOF-PET scanners allow a better localization of the annihilation event thanks to a higher coincidence time resolution, offering a large potential for image quality improvement (Vandenberghe et al., 2016). Brain PET scans were performed using four different neuroimaging radiotracers, namely ^{18}F-FDG, ^{18}F-DOPA, ^{18}F-Flutemetamol and ^{18}F-Flortaucipir, that is 40 patients for each radiotracer. In Table 2.1 the clinical and demographic information of the patients are presented. Table 2.2 provides information regarding the scanning conditions for each radiotracer. The ethics committee of Geneva University Hospitals approved the study protocol and all patients gave informed consent.

	Age (mean, range)	Gender	Indication/Diagnosis
^{18}F-Flortaucipir	66.3 (58-78)	17F/23M	Cognitive symptoms of possible neurodegenerative aetiology
^{18}F-FDG	62.5 (53-81)	25F/15M	
^{18}F-Flutemetamol	63.2 (45-77)	21F/19M	
^{18}F-DOPA	25.4 (20-40)	17F/23M	9 healthy controls 23 patients with a Cannabis use disorder 7 patients with an Internet gaming disorder 1 patient with neuroendocrine tumour

Table 2.1: Demographic and clinical information of patients included in the study.

	Injected dose (MBq) mean±sd	Waiting time (min) mean±sd	Scan duration (min)
^{18}F-Flortaucipir	205 ± 10	76 ± 8	30
^{18}F-FDG	208 ± 14	32 ± 6	20
^{18}F-Flutemetamol	199 ± 11	91 ± 6	20
^{18}F-DOPA	185 ± 12	0	90

Table 2.2: Information about the scan acquisition procedure for each radiotracer.

For all patients, the low-dose CT scan was performed before the PET acquisition using the following parameters:

- 20 mAs, that specifies the flux of x-rays used in the imaging process (Bushberg, 2002),
- 0.3 sec/rotation, that indicates the rotation speed of the x-ray tube during helical scanning,
- pitch of 1, that indicates there is overlap between adjacent acquisitions (Raman et al., 2013),
- 120 kVp, that is the electrical potential applied to each electron as it accelerates in the x-ray tube,
- $0.9 \times 0.9 \times 2.5$ mm^3 that is the voxel size of the CT image.

The reconstruction of the PET images was performed after collecting the PET data using the Siemens e7 tool. An ordinary Poisson-ordered subsets-expectation maximization reconstruction with TOF information (TOF OP-OSEM) was employed, adopting the parameters used in clinical practice (5 iterations, 21 subsets). In the reconstruction process, PET images are formed from the raw data previously collected and in sinogram format by the PET scanner (Figure 2.1). Each time an annihilation event occurs, the line of response (LOR) defines the path where it took place, but its specific location cannot be directly determined. A sinogram is a two-dimensional plane in which each LOR is plotted as function of its angular orientation from the center (y-axis) versus its distance from the center (x-axis) (Fahey, 2002). PET images were separately reconstructed 2 times:

- the first time without attenuation and scatter correction in order to generate uncorrected PET images (PET-nonAC images),

- the second time employing the single scatter simulation (SSS) algorithm with tail fitting for scaling in order to generate the attenuation and scatter corrected PET images using CT information (PET-CTAC images).

The reconstructed PET images consists of a $200 \times 200 \times 109$ matrix with a voxel size of $2 \times 2 \times 2$ mm^3. To improve image quality through reducing the noise, a Gaussian filter with 2 mm FWHM was subsequently applied to all images.

Furthermore, a segmentation-based attenuation map (SegAC) similar to the one implemented on the commercial PET/MRI system was used as a proxy for comparative evaluation with the proposed technique. The TOF reconstructed PET-nonAC images were segmented in 2 classes: background air and soft-tissue. The contour of the head was delineated using thresholding and then attenuation coefficients of 0.1 cm^{-1} and 0.0 cm^{-1} were assigned to voxels located inside and outside the head contour, respectively.

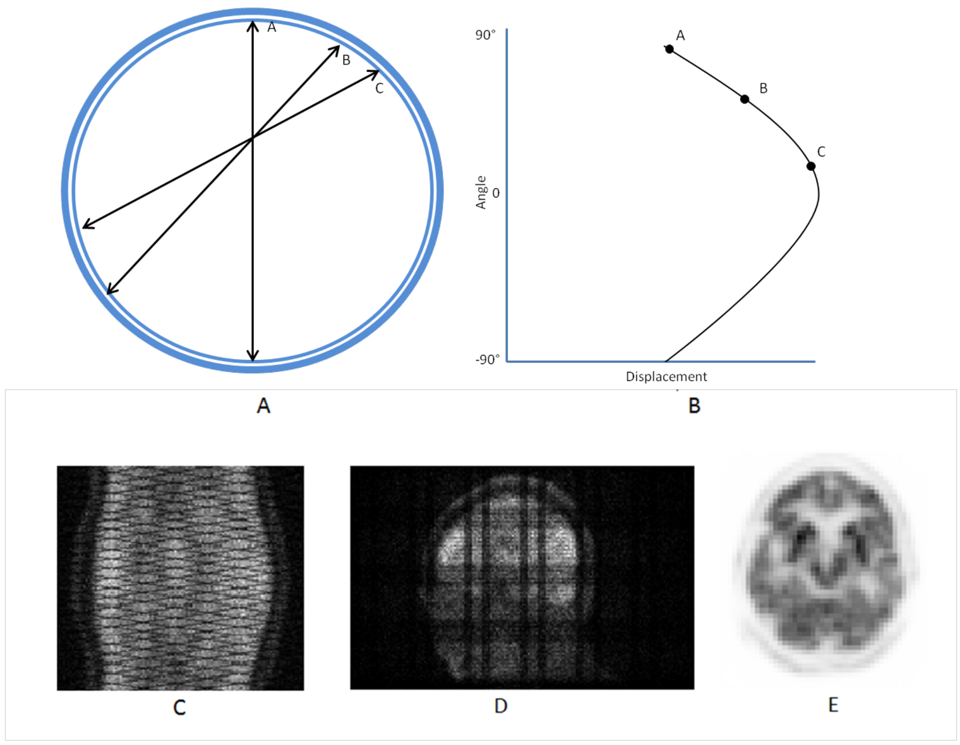

Figure 2.1: In subfigure A the blue circle represents the ring of detectors and the four black lines indicate the lines of response of 4 different annihilation events. The LORs are plotted in a two-dimensional space where in the x-axis there is the displacement from the center and in the y-axis there is the angular orientation (subfigure B). In subfigure C and D the sinogram representing more complicated patterns of LORs, such as a sinogram of brain scans, composed of many overlapping sine waves, is shown. After reconstruction, PET images corresponding to this sinogram are obtained (subfigure E).

2.2 Network architecture

A deep convolutional neural network was employed to predict PET attenuation and scatter corrected (PET-DLAC) images from uncorrected (PET-nonAC) images in an end-to-end fashion. Convolutional neural networks are inspired from the complex hierarchical structure of neurons and connections in the brain. The basic unit of computation is the neuron and more neurons together compose multiple processing layers (LeCun, Bengio, and Hinton, 2015). The neuron receives information from an external source in the input layer or from other layers and sends information to other neurons in the following layers. Each neuron connection has an associated weight, which is assigned on the basis of its relative importance to other connections and there are some forms of 'learning rules' which modify the weights according to the input patterns. The main characteristic of the convolutional neural networks is the ability to recognize visual patterns directly from pixel images with minimal preprocessing, thanks to a series of convolutions and pooling operations during which the features are detected (Krizhevsky, Sutskever, and Hinton, 2012). Implementation of the deep learning algorithm was carried out using the open-source convolutional neural network platform, called Niftynet. It offers a modular deep-learning platform for common medical imaging applications, enabling the rapid implementation of deep learning solutions based on state-of-the-art convolutional neural network architectures (Gibson et al., 2018). It is built on the TensorFlow framework (version 1.12) that provides a programming interface in Python (version 3.6). The implemented network is the so-called highresnet convolutional neural network, developed originally for volumetric image segmentation (Li et al., 2017), trained using the net_regress application for deep learning-based image regression. The network consists of 20 convolutional layers:

- in the first seven layers a convolution kernel of 3×3×3-voxel is applied in order to encode low-level features, such as edges and corners from the input image,
- in the subsequent seven layers, the kernel is dilated by a factor of two to capture medium-level features,

- in the last six convolutional layers, the kernel is dilated by a factor of four to capture high-level features.

A residual connection links each couple of consecutive convolutional layers that are connected to a batch normalization layer and an element-wise rectified linear unit (ReLU). This residual network framework aims to create identity mapping connections in order to bypass some parametrized layers in the network and render optimization easier (He et al., 2016). Moreover, the residual blocks with identity mapping enable the direct fusion of features from different levels. Lastly, the ReLU, batch normalisation, and convolutional layers are arranged in the pre-activation order to make training easier and to improve generalisation. The whole architecture is illustrated in Figure 2.2.

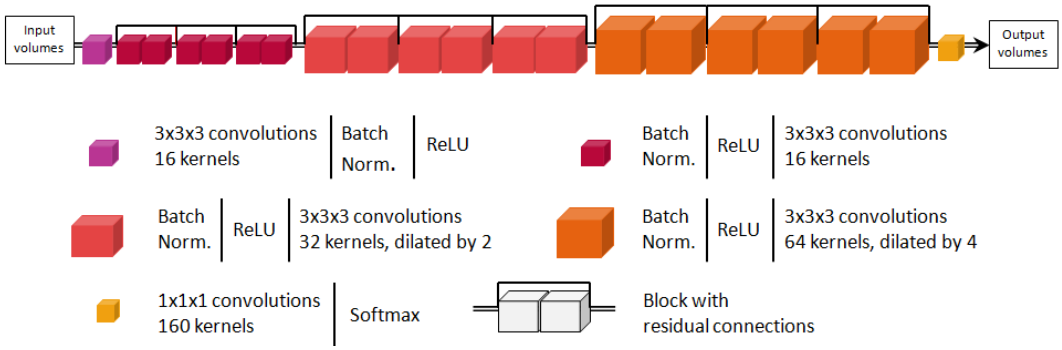

Figure 2.2: The architecture of the network is characterized by 20 convolutions layers that are built in order to extract different types of features from the input images. The layers are organized in a residual network framework.

2.3 Training and optimization

In the first step, the voxel values of PET-CTAC and PET-nonAC images were converted to standardized uptake value (SUV) scale. SUV values are used in clinical practice to quantify the radiotracer uptake considering the patient's weight and the injected activity using the following formula (Gunderson and Tepper, 2015)

$$SUV_i = \frac{C_i}{ID/BW}, \tag{2.1}$$

where C_i is the activity concentration expressed in MBq/mL, ID is the injected activity expressed in MBq and BW is the patient's body weight on the day of imaging expressed in grams. Subsequently, in order to reduce the range of the SUV values, the intensities of PET images were scaled down using a fixed normalization factor separately for each radiotracer. The values of the normalization factors are presented in Table 2.3.

PET radiotracer		**Scaling factor**
^{18}F-FDG	PET-CTAC	10
	PET-nonAC	2.1
^{18}F-DOPA	PET-CTAC	3
	PET-nonAC	1
^{18}F-Flutemetamol	PET-CTAC	1.5
	PET-nonAC	0.3
^{18}F-Flortaucipir	PET-CTAC	1.8
	PET-nonAC	0.7

Table 2.3: Normalization factors used to reduce the range of SUV values for PET-CTAC and PET-nonAC images for each radiotracer.

There has been no normalization to the mean of radiotracer uptake in the cerebellum and pons (Vemuri et al., 2017). This kind of normalization is usually done in clinical practice for most radiotracers, except for ^{18}FDG. It was not performed herein because it tends to undermine the assessment by hiding the actual underestimation/overestimation of tracer uptake (Figure 2.3). Finally, all PET images were cropped to $128 \times 128 \times 105$ voxels to remove the background air in order to reduce the computational burden by maintaining only the relevant voxels.

The training and evaluation of the convolutional neural network was performed separately for each of the four neuroimaging radiotracers. The specific parameters that have been set are reported in Table 2.4. For the training, a five-fold cross-validation scheme was employed. Therefore, in each of the four datasets, the 40 3D brain images were divided in 5 groups, each group is used as a testing set while the others are used for training. As such, the quantitative analysis was performed on all 40 patients for each neuroimaging radiotracer.

During the training part, both PET-nonAC images and PET-CTAC images are provided to the network and the weights are updated during the iterations in order to maximize the conversion results. Subsequently in the test part, only PET-nonAC images are given to the trained network and it generates PET-DLAC images based on what it learned during the training phase.

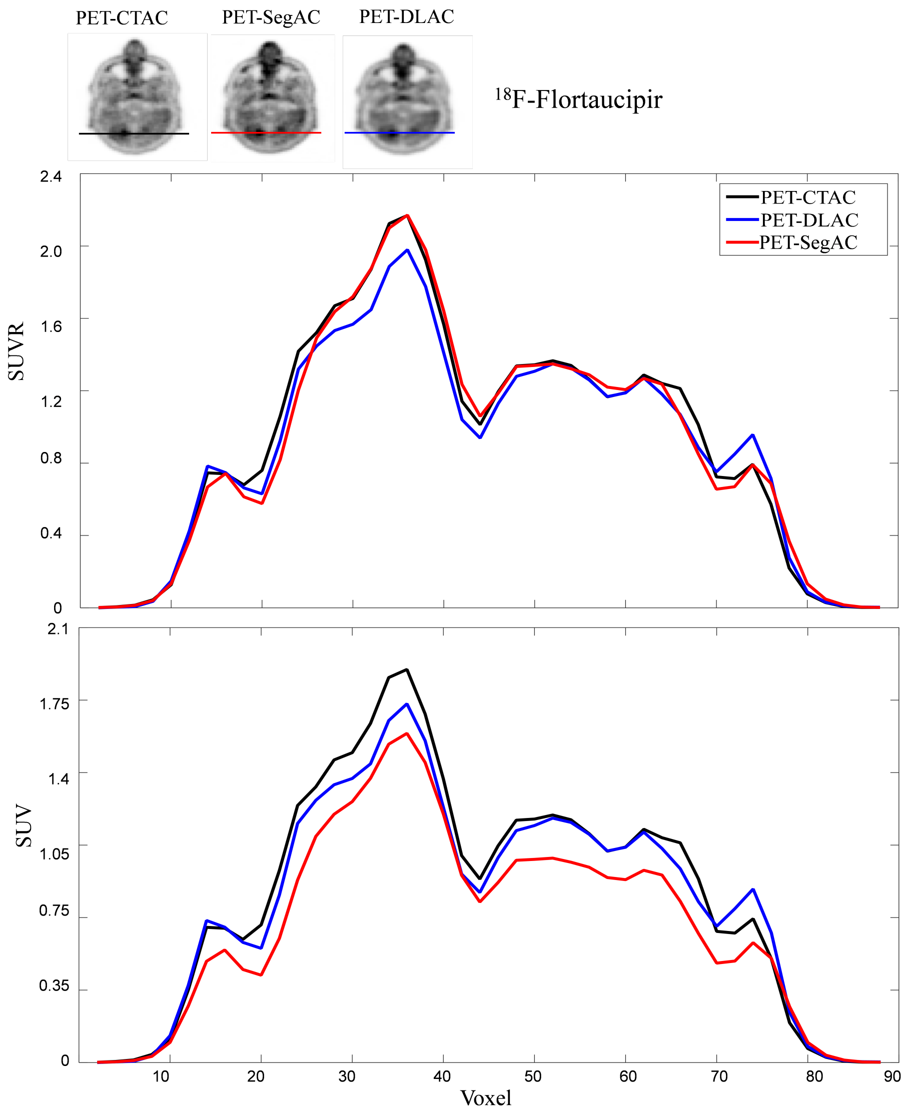

Figure 2.3: The three PET images represent the transaxial views of PET-CTAC, PET-SegAC and PET-DLAC for ^{18}F-Flortaucipir. The colored lines delineate the three brain regions for which the SUV and SUVR profiles are presented in the two panels below. SUVR values are obtained by the normalization of the SUV PET images via mean SUV of the cerebellum. The SegAC method resulted in noticeable under-estimation of SUV values in the second panel, while the SUVR values in the first panel fictitiously compensated the under-estimated SUV values.

The network was trained in both 2-dimensional (2D) mode and 3-dimensional (3D) mode using a spatial window of 128$\times$128 and 128$\times$128$\times$64 respectively. The results of the quantitative analysis was slightly better for the 2D mode and therefore only the results for this mode are reported in the following chapter.

Parameter	Value
Spatial window It specifies the input window size for the convolutional neural network	128 × 128
Learning rate It is a scalar used to update model parameters during optimization loops	0.002
Optimizer It is a function that updates the weight parameters to minimize the loss function	Adam
Loss function It is a function used to compute the difference between the input and the output of the network	L2norm
Decay It is a scalar that determines the strength of regularisation	0.0001
Batch size It is a scalar that indicates the number of images to be processed at each iteration of the algorithm	120
Sample per volume It is a scalar that indicates the number of samples to take from each image volume	1

Table 2.4: Principal parameters of the convolutional neural network and their corresponding values.

2.4 Data analysis

For quantitative assessment, the CTAC method was considered as reference for evaluation of the deep learning (DLAC) and the segmentation (SegAC) methods. To this end, different calculations were performed for (i) the entire head, (ii) the three main tissue classes and (iii) for specific brain regions identified on tracer-specific atlases.

To obtain the main three tissue types, the CT images were segmented for values higher than 160 HU for bone, lower that -400 HU for air cavities within the head contour and between -400 HU and 160 HU for soft tissue. HU is the Hounsfield unit, which describes the radiodensity of tissues in CT images. For the entire head and for the main three tissue classes, the measures that have been used are mean error (ME) in Eq. 2.2, mean absolute error (MAE) in Eq. 2.3, root mean square error (RMSE) in Eq. 2.4 and relative error (RE(%)) in Eq. 2.5.

$$ME = \frac{1}{v}\sum_{i=1}^{v} PET_{test}(i) - PET_{ref}(i) \tag{2.2}$$

$$MAE = \frac{1}{v}\sum_{i=1}^{v} |PET_{test}(i) - PET_{ref}(i)| \tag{2.3}$$

$$RMSE = \sqrt{\frac{1}{v}\sum_{i=1}^{v}(PET_{test}(i) - PET_{ref}(i))^2} \tag{2.4}$$

$$RE(\%) = \frac{(PET_{test})_i - (PET_{ref})_i}{(PET_{ref})_i} \times 100\% \tag{2.5}$$

In the above equations PET_{test} stands for corrected PET images using either the deep learning-based or the segmentation method, i indicates the voxel index and v the total number of voxels. Moreover, peak signal-to-noise ratio (PSNR) and structural similarity index (SSIM) metrics were computed to assess the similarity and accuracy of the generated PET images using Eqs. 2.6 and 2.7, respectively.

$$PSNR(dB) = 10\log_{10}(\frac{Mv^2}{MSE}), \tag{2.6}$$

$$SSIM = \frac{(2Mn_{ref}Mn_{test} + K_1)(2\delta_{ref,test} + K_2)}{(Mn_{ref}^2 + Mn_{test}^2 + K_1)(\delta_{ref}^2 + \delta_{test}^2 + K_2)}. \tag{2.7}$$

In Eq. 2.6, Mv indicates the maximum intensity value of PET_{ref} or PET_{test} images whereas

$$MSE = \frac{1}{v}\sum_{i=1}^{v}(PET_{test}(i) - PET_{ref}(i))^2, \tag{2.8}$$

is the mean squared error. In Eq. 2.7, Mn_{ref} is the mean value of PET_{ref} and Mn_{test} image is the mean value of the PET_{test} image. δ_{ref} and δ_{test}t are the variances of PET_{ref} and PET_{test} images where their covariance is denoted by $PET_{ref,test}$. To avoid a division by a very small value, K_1=0.01 and K_2=0.02 were inserted in Eq. 2.7.

Depending on the radiotracer, specific brain regions have been defined in the following way:

- For ^{18}F-FDG, the Hermes BRASS analysis tool (Hermes Medical Solutions AB, Sweden) was used to define 63 brain regions;
- For ^{18}F-Flortaucipir and ^{18}F-Flutemetamol radiotracers in-house developed tracer-dependent templates were used to spatially normalize the PET images to the Montreal Neurological Institute (MNI) reference space (Evans et al., 1993) and 70 regions have been defined. The defined regions in this case are 70 instead of the 134 provided by the MNI template because the left and right regions were merged.

- For ^{18}F-DOPA radiotracer, PET images were also spatially normalized to MNI reference space using a publicly available ^{18}F-DOPA-PET template (Gómez et al., 2018) and only 6 clinically relevant regions were mantained: posterior, frontal, cerebellum, right and left caudate, right and left putamen.

For these specific regions of the brain, the relative error in Eq. 2.9 (RE(%)) and the absolute relative error in Eq 2.10 (ARE(%)) have been used.

$$RE_{region}(\%) = \frac{(PET_{test})_{region} - (PET_{ref})_{region}}{(PET_{ref})_{region}} \times 100\% \tag{2.9}$$

$$ARE_{region}(\%) = |\frac{(PET_{test})_{region} - (PET_{ref})_{region}}{(PET_{ref})_{region}}| \times 100\% \tag{2.10}$$

A paired t-test analysis was also employed to evaluate statistical significance of the differences between the calculated metrics for the segmentation and deep learning methods. A p-value less than 0.05 was considered statistically significant.

In addition, a joint histogram analysis that allows the visualization of the relationship between the values of corresponding voxels in two images was included. In this case, the correlation between the voxel-wise radiotracer activity distribution of PET-DLAC images or PET-SegAC images against the PET-CTAC images (Hill and Hawkes, 2000) has been displayed for each PET neuroimaging radiotracer.

Lastly, the 160 PET-DLAC images were visually inspected in order to identify any gross errors in the determination of the SUV uptake and the specific cases were separately reported.

Chapter 3

Results

For each of the four radiotracers, ME, MAE, RE, RMSE, PSNR and SSIM metrics for the entire head are reported in Table 3.1. The quantitative evaluation compares PET-DLAC and PET-SegAC images with PET-CTAC images, and both results are reported separately. The DLAC method presents lower values for the measured errors compared to the SegAc approach and the p-values of the paired t-test between the two results were statistically significant ($p<0.04$) for all metrics, apart from PSNR and SSIM.

^{18}F-Flortaucipir	**ME (SUV)**	**MAE (SUV)**	**RE (%)**	**RMSE (SUV)**	**PSNR (dB)**	**SSIM**
PET-DLAC	-0.02±0.01	0.08±0.02	3.6±4.9	0.09±0.02	34.7±3.8	0.96±0.02
PET-SegAC	-0.30±0.06	0.41±0.08	-6.2±4.0	0.45±0.08	31.9±3.7	0.92±0.02
^{18}F-Flutemetamol						
PET-DLAC	-0.01±0.01	0.05±0.01	2.1±3.3	0.07±0.02	36.0±3.6	0.97±0.02
PET-SegAC	-0.26±0.05	0.36±0.07	-6.0±3.9	0.42±0.07	32.7±3.5	0.93±0.02
^{18}F-FDG						
PET-DLAC	0.12±0.75	0.18±0.46	3.1±6.9	0.2±0.38	34.2±3.3	0.94±0.02
PET-SegAC	-0.40±0.35	0.42±0.30	-6.4±5.8	0.51±0.29	32.1±3.2	0.90±0.03
^{18}F-DOPA						
PET-DLAC	-0.11±0.68	0.17±0.39	3.9±6.9	0.2±0.37	34.9±3.1	0.94±0.02
PET-SegAC	-0.37±0.32	0.40±0.28	-7.1±6.1	0.49±0.27	32.3±3.0	0.91±0.03

Table 3.1: Summary of performance evaluation of the DLAC and SegAC methods in the entire head. For each metric, the mean and the standard deviation calculated among the 40 PET images for each dataset are provided.

For each radiotracer the ME, MAE and RE metrics are reported for the three main types of tissue (soft tissue, air cavities and bones) in Table 3.2. The quantitative values generated by the DLAC approach are lower than those produced by SegAC. The results are statistically different ($p < 0.05$) between the two methods, except the ME in soft-tissue for ^{18}F-Flutemetamol ($p=0.06$).

	^{18}F-Flortaucipir			^{18}F-Flutemetanol		
Soft-tissue	**ME (SUV)**	**MAE (SUV)**	**RE (%)**	**ME (SUV)**	**MAE (SUV)**	**RE (%)**
PET-DLAC	-0.02±0.01	0.05±0.02	2.0±4.2	-0.01±0.01	0.07±0.02	2.2±3.7
PET-SegAC	0.08±0.05	0.16±0.07	3.3±3.9	0.07±0.04	0.15±0.06	3.5±3.9
Bone						
PET-DLAC	-0.03±0.02	0.06±0.03	-1.9±6.2	-0.03±0.03	0.07±0.07	-2.0±6.4
PET-SegAC	-0.18±0.05	0.20±0.05	-7.0±6.7	-0.17±0.06	0.22±0.06	-7.1±6.8
Air cavity						
PET-DLAC	0.02±0.11	0.03±0.10	4.0±6.5	0.03±0.12	0.04±0.11	4.2±6.6
PET-SegAC	0.11±0.21	0.12±0.19	24.2±8.4	0.13±0.23	0.15±0.19	26.3±9.0

	^{18}F-FDG			^{18}F-DOPA		
Soft-tissue	**ME (SUV)**	**MAE (SUV)**	**RE (%)**	**ME (SUV)**	**MAE (SUV)**	**RE (%)**
PET-DLAC	0.11±0.69	0.17±0.45	1.9±5.7	-0.09±0.61	0.15±0.39	-2.8±5.9
PET-SegAC	-0.39±0.33	0.41±0.30	-4.1±6.7	-0.31±0.29	0.39±0.27	-4.9±6.0
Bone						
PET-DLAC	0.08±0.52	0.10±0.47	1.8±7.1	-0.07±0.48	0.09±0.42	-1.9±6.4
PET-SegAC	-0.29±0.26	0.30±0.26	-14.0±6.6	-0.26±0.25	0.29±0.24	-13.1±5.8
Air cavity						
PET-DLAC	0.02±0.12	0.03±0.11	4.2±6.8	0.02±0.10	0.03±0.11	4.4±6.5
PET-SegAC	0.12±0.21	0.13±0.20	37.2±8.9	0.11±0.20	0.13±0.19	38.4±9.0

Table 3.2: Summary of performance evaluation metrics for DLAC and SegAC methods in the different tissue classes: soft-tissue, bone and air cavity. The mean and standard deviation calculated among the 40 PET images are reported for each radiotracer.

The Figures 3.1-3.4 show the absolute relative errors (ARE) for DLAC and SegAC approaches assessed in specific brain regions defined on the different templates. Figure 3.1 depicts the mean absolute relative errors (in percent) of SegAC and DLAC approaches for ^{18}F-Flortaucipir in 70 brain regions across 40 subjects. The bars of the histogram indicate the mean absolute relative error for each brain region, while the two horizontal lines are positioned in correspondence of the minimum and maximum of the absolute relative errors, respectively. The mean absolute bias for the DLAC method barely reaches 8%, while for Seg-AC approach, it increased up to 17%. Furthermore, for all the investigated regions, ARE values of the DLAC method are lower than those of the SegAC method. The difference between the two methods is statistically significant for each region, apart from for the Cerebellum exterior (p=0.09), ITG inferior temporal gyrus (p=0.08) and MSFG superior frontal gyrus (p=0.08).

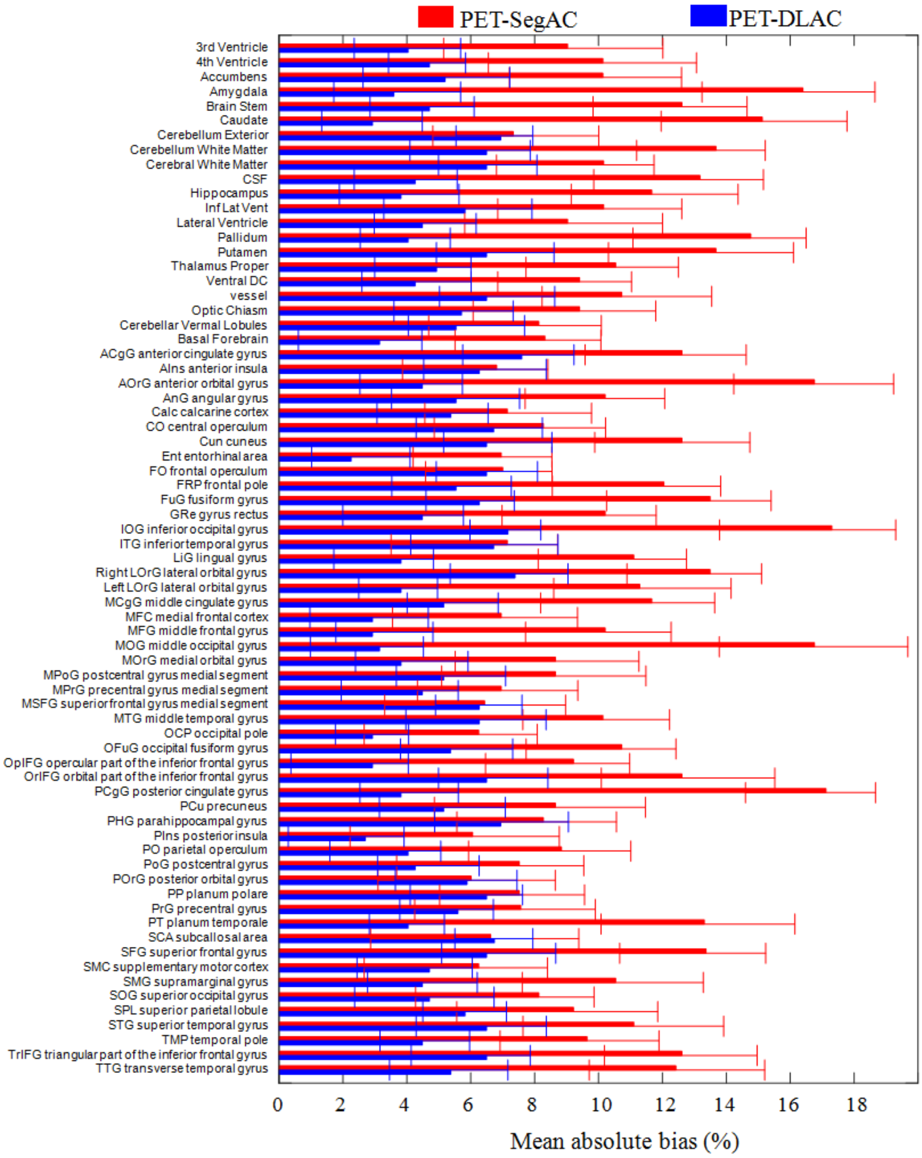

Figure 3.1: Mean absolute relative error (%) calculated for 70 brain regions of PET-DLAC (blue) and PET-SegAC (red) with respect to reference PET-CTAC for ^{18}F-Flortaucipir.

The quantitative accuracy was evaluated using the same metrics in the same brain region also for ^{18}F-Flutemetamol radiotracer. The results are provided in Figure 3.2. Similar to the results of the previous radiotracer, the mean absolute error for the DLAC method reaches 8% in some brain regions, while it reaches almost 16% for the Seg-AC approach. Moreover, for all the considered regions, ARE values of the DLAC are lower than values obtained using the SegAC method. The difference between the two methods is significant ($p<0.05$) for all the involved regions.

In the same way, Figure 3.3 depicts the mean absolute errors in 63 brain regions for DLAC and SegAC approaches applied to ^{18}F-FDG PET images. The DLAC approach leads to an ARE of less than 8%, outperforming in this way the SegAC approach that instead reached 15%. The differences between the DLAC and SegAC approaches were statistically significant, except for the L G.orbitalis (p=0.05).

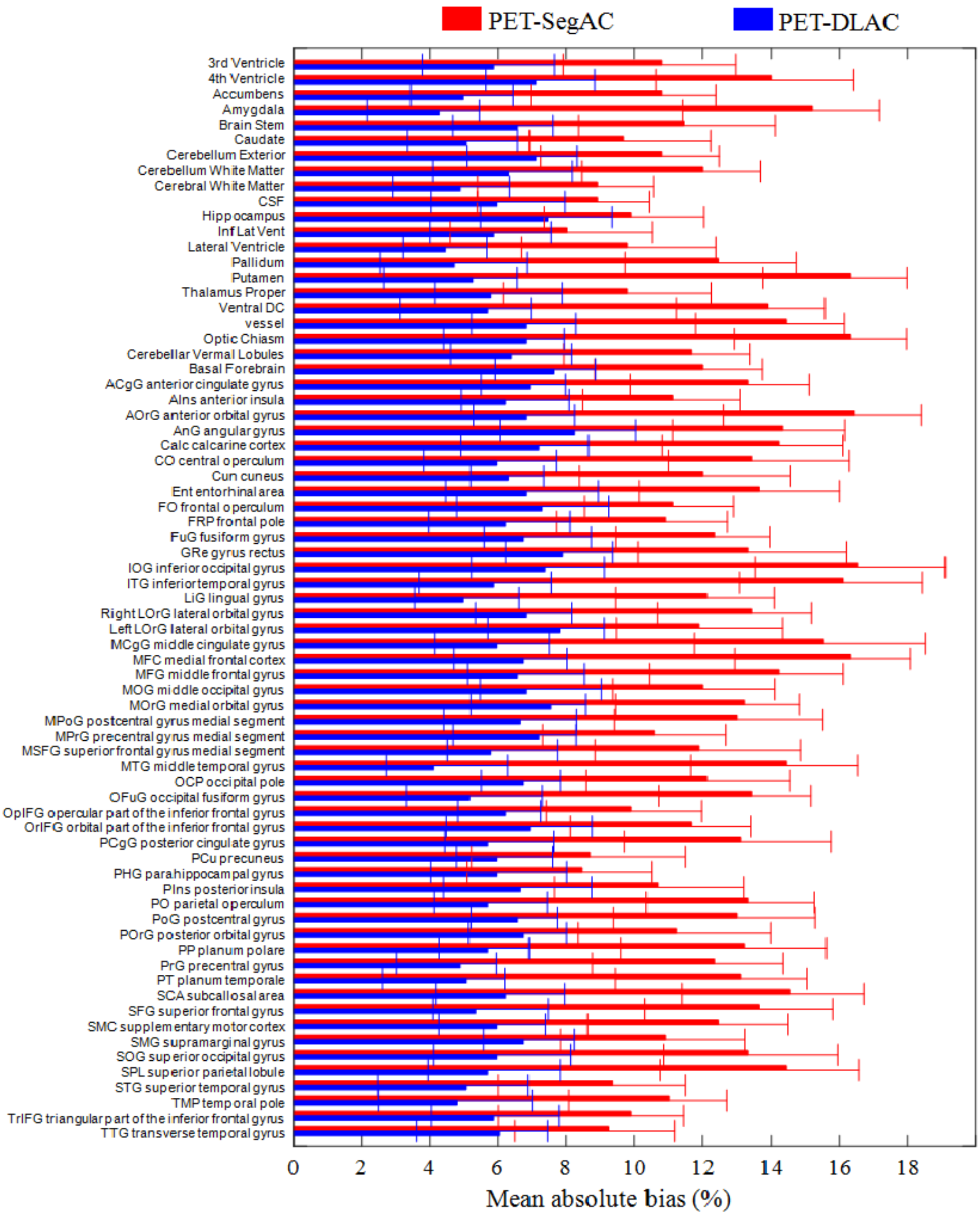

Figure 3.2: Mean absolute relative error (%) calculated for 70 brain regions of PET-DLAC (blue) and PET-SegAC (red) with respect to reference PET-CTAC for ^{18}F-Flutemetamol.

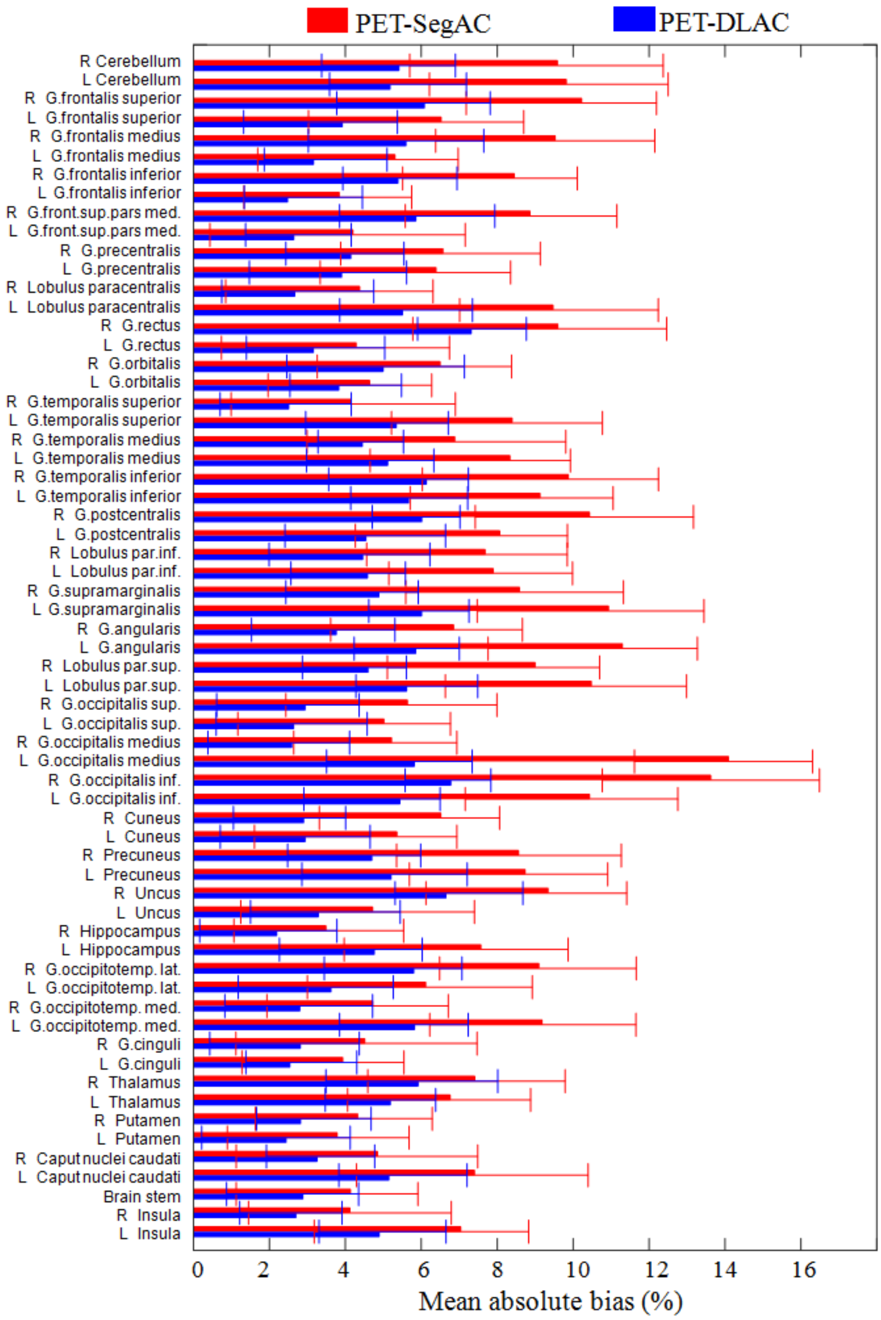

Figure 3.3: Mean absolute relative error (%) calculated for 63 brain regions of PET-DLAC (blue) and PET-SegAC (red) with respect to reference PET-CTAC for ^{18}F-FDG.

Figure 3.4 presents the results of quantitative analysis of DLAC and SegAC approaches for ^{18}F-DOPA PET images within 7 brain regions. One can observe that the DLAC approach outperformed SegAC, leading to less than 8% absolute relative errors. The difference between the two approaches is significant for each region ($p<0.03$).

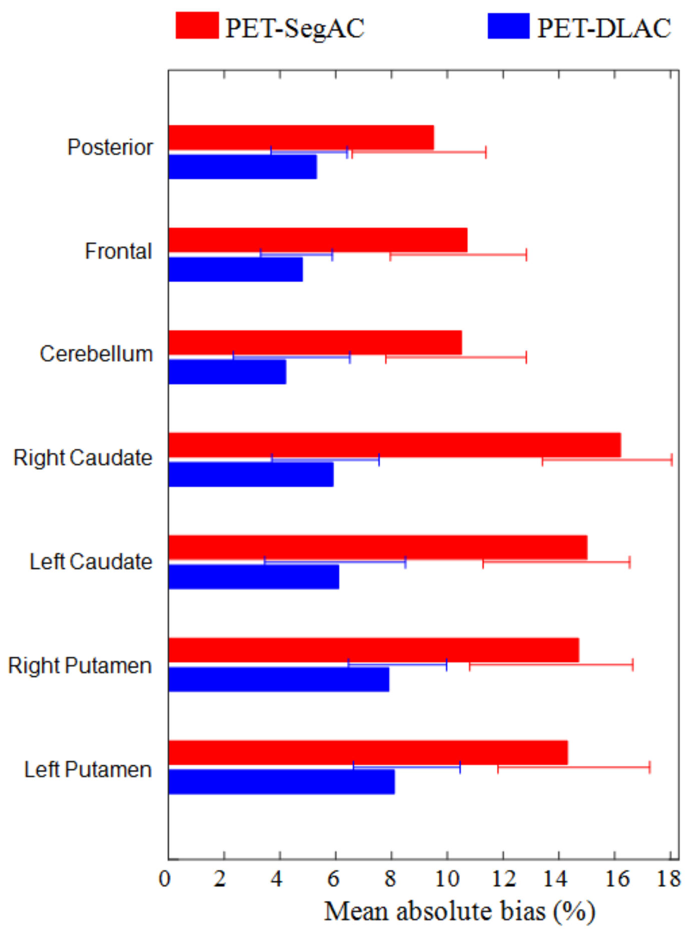

Figure 3.4: Mean absolute relative error (%) calculated for 7 brain regions of PET-DLAC (blue) and PET-SegAC (red) with respect to reference PET-CTAC for ^{18}F-DOPA.

Lastly, in Figure 3.5 the results of the joint histogram analysis of PET-DLAC and PET-SegAC versus reference PET-CTAC images performed over the 40 subjects for each radiotracer are presented. The SegAC method tends to underestimate the uptake values since the slope of the regression line is less than 1. Moreover, in the joint histogram of PET-SegAC versus PET-CTAC images, the points around the lines are more dispersed indicating there is stronger agreement between the estimated and reference images.

In Figure 3.6, an example CT image, corrected PET images using the CT data, SegAC and DLAC methods are presented for each radiotracer. To compare SegAC and DLAC methods, a difference SUV bias map is also shown for each one. This map is based on the difference between the values in the PET-DLAC or PET-SegAC

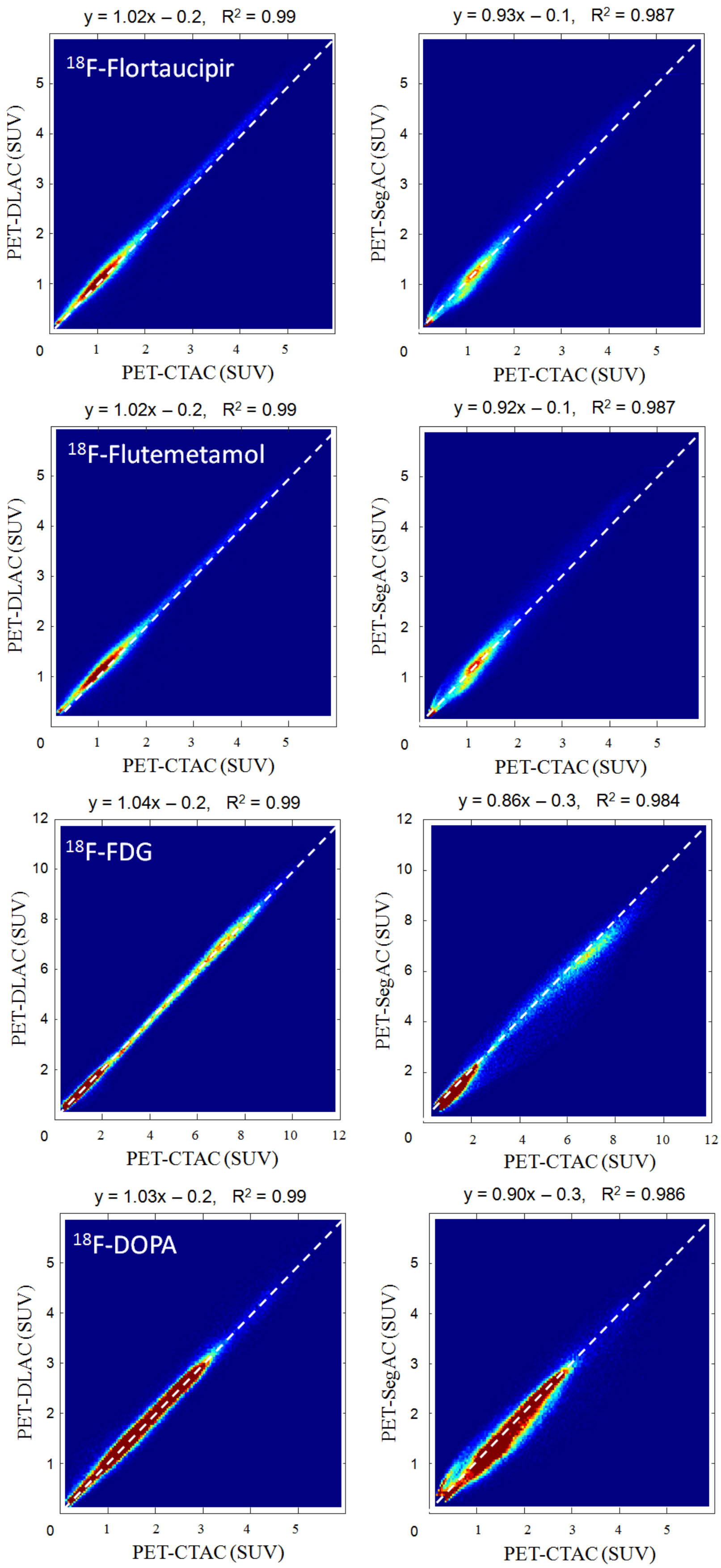

Figure 3.5: Joint histogram of PET-DLAC (first column) and PET-SegAC (second column) versus reference PET-CTAC images performed over the 40 subjects for each radiotracer. In the upper part of the images, the regression line and the squared correlation coefficient (R^2) are presented.

image and the corresponding values in the PET-CTAC image. The red regions indicate overestimation, while the blue regions show underestimation of the considered method against the reference.

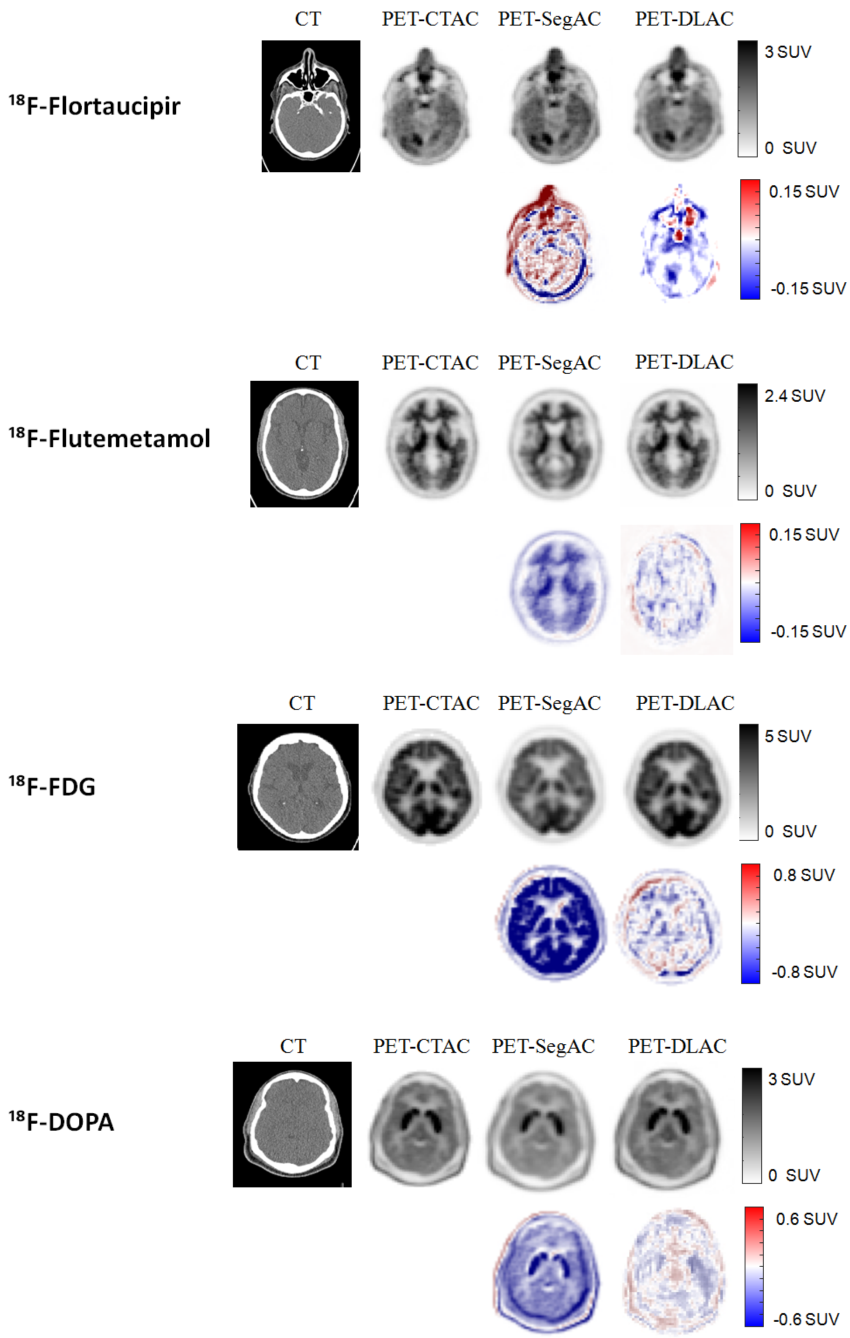

Figure 3.6: For each radiotracer, the first row of images contains the slice of CT image (first from the left), PET-CTAC image (second), PET-SegAC image (third), PET-DLAC image (fourth). In the second row, the difference SUV error map relative to SegAC and PET-DLAC methods are presented (first and second image from the left).

Despite the promising results of the DLAC method showed in the previous tables and figures, PET images of 160 subjects were carefully investigated looking for potential gross errors. Six PET-DLAC images with gross quantification errors were reported: two of them were observed for ^{18}F-FDG and ^{18}F-DOPA, while only one was identified for ^{18}F-Flortaucipir and ^{18}F-Flutemetamol.

In Figure 3.7, PET images of the only outlier observed for ^{18}F-Flortaucipir are shown with the corresponding SUV intensity profiles. The remarkable overestimation of tracer uptake in the posterior region of the PET-DLAC image is noticeable from the red spot in the DLAC bias map and from the blue SUV values intensity profile.

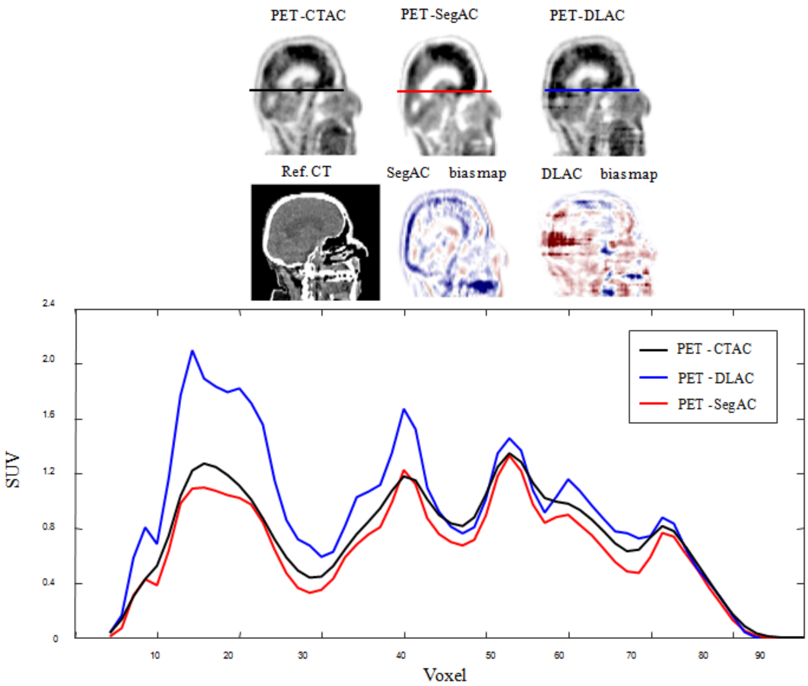

Figure 3.7: Outlier among ^{18}F-Flortaucipir PET images. Sagittal views of PET-CTAC, PET-SegAC, PET-DLAC are presented with their corresponding SUV bias maps. The plot shows SUV profiles in the region delineated by the colored lines in the PET images: black for PET-CTAC, red for PET-SegAC, blue for PET-DLAC. The DLAC approach resulted in considerable overstimation of tracer uptake in the posterior part of the brain.

On the contrary, in Figure 3.8 the DLAC algorithm underestimated the activity uptake in one ^{18}F-Flutemetamol PET image. The underestimation is clearly visible from from the intensity profiles and the blue spot in the DLAC bias map within the soft-tissue region surrounded by bony structures.

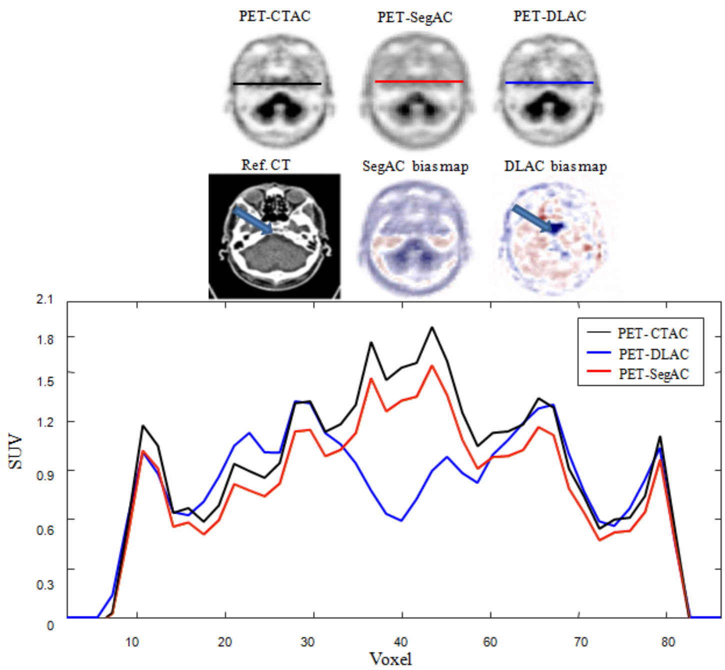

Figure 3.8: Outlier among ^{18}F-Flutemetamol PET images. Transaxial views of PET-CTAC, PET-SegAC, PET-DLAC are presented with their corresponding SUV bias maps. The plot shows SUV profiles in the region delineated by the colored lines in PET images: black for PET-CTAC, red for PET-SegAC, blue for PET-DLAC. The DLAC approach resulted in considerable underestimation of tracer uptake within an area between soft-tissue and bone.

Figure 3.9 also presents another example of underestimation of the tracer uptake generated by the DLAC method in an ^{18}F-FDG PET image within a region consisting of soft-tissue and bone. The other case found among the ^{18}F-FDG PET images is very similar to this one.

Lastly, in Figure 3.10 the overestimation by the DLAC method in a ^{18}F-DOPA PET image is shown in a region containing mostly air. The DLAC approach erroneously attributed an elevated tracer uptake to a similar region also in the second outlier found among the ^{18}F-DOPA PET images.

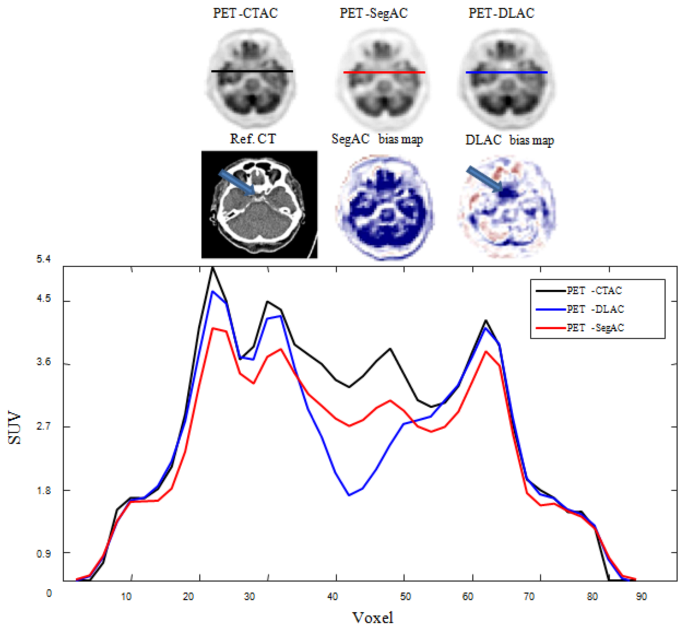

Figure 3.9: Outlier among ^{18}F-FDG PET images. Transaxial views of PET-CTAC, PET-SegAC, PET-DLAC are presented with their corresponding SUV bias maps. The plot shows SUV profiles in the region delineated by the colored lines in PET images: black for PET-CTAC, red for PET-SegAC, blue for PET-DLAC. The DLAC approach resulted in considerable underestimation of tracer uptake within an area between soft-tissue and bone.

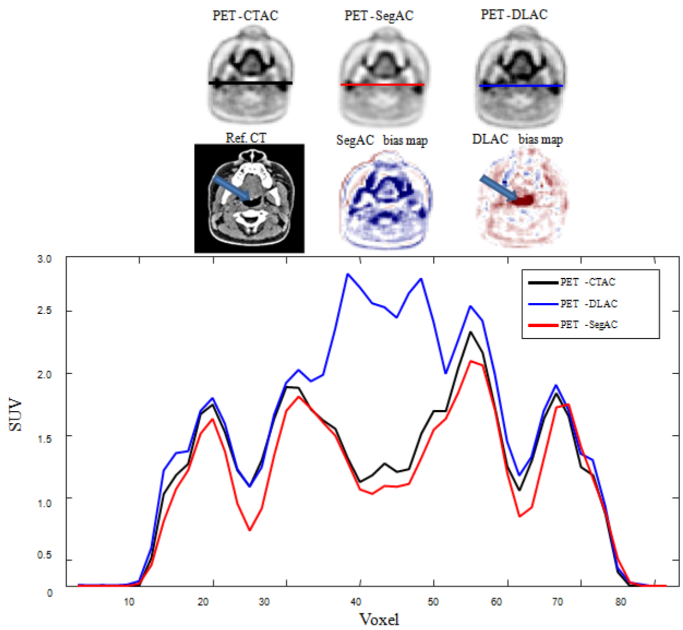

Figure 3.10: Outlier among ^{18}F-DOPA PET images. Transaxial views of PET-CTAC, PET-SegAC, PET-DLAC together with their corresponding SUV bias maps along with reference CT image are presented. The plot shows SUV profiles in the region delineated by the colored lines in PET images: black for PET-CTAC, red for PET-SegAC, blue for PET-DLAC. The DLAC approach resulted in considerable overestimation of tracer uptake within an area located on air canal.

Chapter 4

Discussion

In this study, the quantitative assessment of a deep learning (DLAC) approach for attenuation and scatter correction of brain PET images has been performed. The main characteristic of this correction method is the one-step process in image-space that allows to directly correct PET images for attenuation and scatter without the use of anatomical imaging. A highresnet convolutional neural network was trained in a 5-fold cross validation scheme separately for each radiotracer dataset. Subsequently, the quantitative accuracy of the 160 3D brain images (40 for each radiotracer) has been computed to evaluate the performance of this approach. Moreover, a segmentation (SegAC) method was included in the quantitative evaluation as a bottom line of clinically tolerable errors.

The results of the quantitative analysis showed a clinically acceptable performance of the DLAC with mean RE values of 3.6±4.9%, 2.1±3.3%, 3.1±6.9% and 3.9±6.9% for the ^{18}F-Flortaucipir, ^{18}F-Flutemetamol, ^{18}F-FDG and ^{18}F-DOPA, respectively. Given these results, the approach performed similarly for all radiotracers, independently from the specificity of each radiotracer distribution. Moreover, the mean RE was reduced when using the DLAC approach compared to SegAC which instead resulted in the following results: -6.2±4%, -6±3.9%, -6.4±5.8% and -7.1±6.1% for the ^{18}F-Flortaucipir, ^{18}F-Flutemetamol, ^{18}F-FDG and ^{18}F-DOPA, respectively. In addition, in this case, the superior performance of this approach was equally observed in PET images acquired with the different neuroimaging radiotracers and the results of the paired t-test between the two methods were statistically significant ($p<0.05$), meaning that there is a significant difference in the performance of these two approaches. The difference in the performance of the two approaches is even more visible in the quantitative assessment of the different brain regions. In fact, a mean absolute relative error of less than 8% was achieved when using the DLAC approach while SegAC achieved a mean relative error over 16%. Lastly, the joint histogram analysis showed the tendency of the DLAC method to overestimate the tracer uptake and the lower dispersity of the voxel values compared to the SegAC approach. Particular attention was given to potential susceptibility of the DLAC approach to outliers and for this reason the entire dataset was carefully examined. Six PET-DLAC images with gross errors have been found, equally distributed among the different radiotracer dataset since no evident link between the outliers and a specific radiotracer was observed. The training of the algorithm was performed in both 2D and 3D modes and interestingly 3D training resulted in the same type of artefacts in the patients shown in figures 3.8-3.10. In addition, other similar types of artefacts were found in other patients. The 3D mode didn't generate gross errors in Figure 3.7 and as such, these could be attributed to technical failure of the deep learning approach, whereas the other three outliers may be linked to a misalignment between CT and PET images. Moreover, the weak information about anatomical structures contained in the PET-nonAC images could also challenge the deep learning algorithm to effectively recover the actual activity concentration.

Recently, two other studies (Shiri et al., 2019, Yang et al., 2019) investigated the performance of a deep learning approach for attenuation and scatter correction of ^{18}F-FDG PET images using a deep convolutional encoder-decoder (Cho et al., 2014). For the entire head, a mean RE of -0.1$\pm$2.14% (ranging from -9.5% to 10.0%) calculated over 18 patients was reported by Shiri et al., 2019 whereas a mean RE of 3.98$\pm$15.42% over 10 patients was reported in Yang et al., 2019. In this last study, when the outlier was removed, the mean RE substantially was reduced to 0.2$\pm$01.92% over 9 patients. However, the results from these two studies are not directly comparable with the results of the present work, first because the deep learning architecture employed in Yang et al., 2019 and Shiri et al., 2019 consist of deep convolution encoder-decoders, keeping in mind that in deep learning approaches, the architecture plays a crucial role. Secondly, the number of patients involved in the studies and the variability among the patients are critical for the outcome of the analysis.

CT imaging provides a straightforward solution for accurate attenuation and scatter correction. However, improvements in correction techniques have been made in cases in which only MRI is available. Regarding the use of the DLAC approach as a possible alternative to MRI-based attenuation correction in PET/MRI, it is necessary to distinguish between clinical practice and literature. Vendor-implemented MR-AC methods for the brain currently present a mean RE higher than 10% (Hofmann et al., 2011, Martinez-Möller et al., 2009b, Mehranian, Arabi, and Zaidi, 2016a). On the other hand, in a recent study (Ladefoged et al., 2017) in which a selection of 11 different MR-based attenuation correction methods for brain PET images was evaluated on a unified subject cohort with identical metrics and common CT-based reference, the mean RE values in PET tracer uptake was within $\pm 5\%$ for all the investigated methods. Therefore, the DLAC method could improve the accuracy of the correction that is made nowadays on PET/MRI scanners in the clinic. Yet, in the literature, there are other more powerful approaches capable of taking advantage of the available structural information from MR imaging.

The use of deep learning methods to obtain a direct correction without the use of anatomical imaging has a big potential because it may offer clinically feasible solutions in cases in which a dedicated PET scanner lacking concurrent structural imaging is accessible, such as a small-FOV PET (Tashima and Yamaya, 2016) or wearable PET technologies (Melroy et al., 2017). In fact, these systems allow significantly higher spatial resolution, but one of the most challenging issue is attenuation correction. Furthermore, one of the advantages of correcting directly in the image-space without the need of anatomical imaging is that the inaccuracies derived from MRI and CT intrasubject mis-registration or different positioning during the scan can be avoided.

In general the convolutional neural network was able to generalize to new data and performed well. Still, despite the promising results achieved by the DLAC method presented in this study, the technique suffers from several limitations. First of all, deep convolutional neural networks are largely dependent on the amount of data and in this study only 32 brain PET images were used for training of the network. A small dataset may generate problems of overfitting and an increase of the size is usually recommended to control these issues (Raudys and Jain, 1991). Moreover, not only the size of the sample, but also its composition plays a decisive role in the performance. The composition should reproduce the heterogeneity of the different types of diseases, such as tumors or other diseases and a bigger dataset that takes into consideration a higher variability of the patients is certainly relevant as a future step for more robust training and evaluation. To be used with other types of radiotracers, the network would need to be retrained on new dataset of PET images scanned with the new radiotracer. This may create some difficulties for certain radiotracers that are not frequently used because it may take long period of time to collect the required amount of PET images. Lastly, the application of deep convolutional neural networks to PET images is challenging because of the low resolution and noise characteristics of PET.

Chapter 5

Conclusion

In this study, a deep learning-based joint PET attenuation and scatter correction (DLAC) was implemented and evaluated separately for four different neuroimaging radiotracers. This approach enables to perform the correction is image-space instead of the sinogram-space, without the need for anatomical imaging. In fact, CT images are essential only in the phase of training of the convolutional neural network, as these are required to learn how the correction is carried out. When the network is trained, PET images corrected for attenuation and scatter are directly generated. In this work, 40 brain PET images for each radiotracer were employed in a 5-cross validation scheme. Thirty-two of the 40 brain PET images were used for training whereas the other 8 were used for testing. This have been repeated independently 5 times using each time 8 brain PET images that were not previously used. The quantitative analysis demonstrated superior performance of the DLAC approach over the segmentation-based (SegAC) method, which approximates the one used in the clinic. Moreover, the DLAC method demonstrated qualitatively and quantitatively acceptable performance for the four different neuroimaging radiotracers investigated, regardless of the radiotracer used. The DLAC method resulted in less than 8% mean absolute relative error compared to the SegAC method, which resulted in more than 16% bias. Despite these promising results, the DLAC approach turned out to be vulnerable to outliers, resulting in image artefacts and large quantification errors. When employing this approach in the clinic, particular attention should be given because it might alter the clinical interpretation of the resulting PET images.

Bibliography

Arabi, Hossein et al. (2015). “Clinical assessment of MR-guided 3-class and 4-class attenuation correction in PET/MR”. In: *Molecular Imaging and Biology* 17.2, pp. 264–276.

Bailey, Dale L et al. (2005). *Positron emission tomography*. Springer.

Benoit, Didier et al. (2016). “Optimized MLAA for quantitative non-TOF PET/MR of the brain”. In: *Physics in Medicine & Biology* 61.24, p. 8854.

Berker, Yannick and Yusheng Li (2016). “Attenuation correction in emission tomography using the emission data—a review”. In: *Medical physics* 43.2, pp. 807–832.

Bushberg, Jerrold T (2002). *The essential physics of medical imaging*. Lippincott Williams & Wilkins.

Chiotis, Konstantinos et al. (2017). “Clinical validity of increased cortical uptake of amyloid ligands on PET as a biomarker for Alzheimer’s disease in the context of a structured 5-phase development framework”. In: *Neurobiology of aging* 52, pp. 214–227.

Cho, Kyunghyun et al. (2014). “On the properties of neural machine translation: Encoder-decoder approaches”. In: *arXiv preprint arXiv:1409.1259*.

Defrise, Michel, Ahmadreza Rezaei, and Johan Nuyts (2012). “Time-of-flight PET data determine the attenuation sinogram up to a constant”. In: *Physics in Medicine & Biology* 57.4, p. 885.

Evans, Alan C et al. (1993). “3D statistical neuroanatomical models from 305 MRI volumes”. In: *1993 IEEE conference record nuclear science symposium and medical imaging conference*. IEEE, pp. 1813–1817.

Fahey, Frederic H (2002). “Data acquisition in PET imaging”. In: *Journal of nuclear medicine technology* 30.2, pp. 39–49.

Gibson, Eli et al. (2018). “NiftyNet: a deep-learning platform for medical imaging”. In: *Computer methods and programs in biomedicine* 158, pp. 113–122.

Gómez, Francisco Javier García et al. (2018). “Elaboración de una plantilla de SPM para la normalización de imágenes de PET con 18F-DOPA”. In: *Imagen Diagnóstica* 9.01, pp. 23–25.

Gunderson, Leonard L, Joel E Tepper, et al. (2015). *Clinical radiation oncology*. Elsevier Health Sciences.

He, Kaiming et al. (2016). “Deep residual learning for image recognition”. In: *Proceedings of the IEEE conference on computer vision and pattern recognition*, pp. 770–778.

Hill, Derek LG and David J Hawkes (2000). “Across-modality registration using intensitybased cost functions”. In: *Handbook of Medical Imaging: Processing and Analysis*, pp. 537–553.

Hofmann, Matthias et al. (2011). “MRI-based attenuation correction for whole-body PET/MRI: quantitative evaluation of segmentation-and atlas-based methods”. In: *Journal of Nuclear Medicine* 52.9, pp. 1392–1399.

Krizhevsky, Alex, Ilya Sutskever, and Geoffrey E Hinton (2012). “Imagenet classification with deep convolutional neural networks”. In: *Advances in neural information processing systems*, pp. 1097–1105.

Kubota, Kazuo (2001). “From tumor biology to clinical PET: a review of positron emission tomography (PET) in oncology”. In: *Annals of nuclear medicine* 15.6, pp. 471–486.

Ladefoged, Claes N et al. (2017). “A multi-centre evaluation of eleven clinically feasible brain PET/MRI attenuation correction techniques using a large cohort of patients”. In: *Neuroimage* 147, pp. 346–359.

LeCun, Yann, Yoshua Bengio, and Geoffrey Hinton (2015). “Deep learning”. In: *nature* 521.7553, p. 436.

Li, Wenqi et al. (2017). “On the compactness, efficiency, and representation of 3D convolutional networks: brain parcellation as a pretext task”. In: *International Conference on Information Processing in Medical Imaging*. Springer, pp. 348–360.

Martinez-Möller, Axel et al. (2009a). "Tissue classification as a potential approach for attenuation correction in whole-body PET/MRI: evaluation with PET/CT data". In: *Journal of nuclear medicine* 50.4, pp. 520–526.

— (2009b). "Tissue classification as a potential approach for attenuation correction in whole-body PET/MRI: evaluation with PET/CT data". In: *Journal of nuclear medicine* 50.4, pp. 520–526.

Mehranian, Abolfazl, Hossein Arabi, and Habib Zaidi (2016a). "Quantitative analysis of MRI-guided attenuation correction techniques in time-of-flight brain PET/MRI". In: *Neuroimage* 130, pp. 123–133.

— (2016b). "Vision 20/20: magnetic resonance imaging-guided attenuation correction in PET/MRI: challenges, solutions, and opportunities". In: *Medical physics* 43.3, pp. 1130–1155.

Melroy, Samantha et al. (2017). "Development and design of next-generation head-mounted ambulatory microdose positron-emission tomography (AM-PET) system". In: *Sensors* 17.5, p. 1164.

Montandon, Marie-Louise and Habib Zaidi (2005). "Atlas-guided non-uniform attenuation correction in cerebral 3D PET imaging". In: *Neuroimage* 25.1, pp. 278–286.

Newberg, Andrew, Abass Alavi, and Martin Reivich (2002). "Determination of regional cerebral function with FDG-PET imaging in neuropsychiatric disorders". In: *Seminars in nuclear medicine*. Vol. 32. 1. Elsevier, pp. 13–34.

Pantaleo, MA et al. (2008). "Conventional and novel PET tracers for imaging in oncology in the era of molecular therapy". In: *Cancer treatment reviews* 34.2, pp. 103–121.

Politis, Marios and Paola Piccini (2012). "Positron emission tomography imaging in neurological disorders". In: *Journal of neurology* 259.9, pp. 1769–1780.

Raman, Siva P et al. (2013). "CT scan parameters and radiation dose: practical advice for radiologists". In: *Journal of the American College of Radiology* 10.11, pp. 840–846.

Raudys, Sarunas J and Anil K. Jain (1991). "Small sample size effects in statistical pattern recognition: Recommendations for practitioners". In: *IEEE Transactions on Pattern Analysis & Machine Intelligence* 3, pp. 252–264.

Shim, Sung Shine et al. (2005). “Non–small cell lung cancer: prospective comparison of integrated FDG PET/CT and CT alone for preoperative staging”. In: *Radiology* 236.3, pp. 1011–1019.

Shinotoh, Hitoshi and Donald B Calne (1995). “The use of pet in parkinsons-disease”. In: *Brain and cognition* 28.3, pp. 297–310.

Shiri, Isaac et al. (2019). “Direct attenuation correction of brain PET images using only emission data via a deep convolutional encoder-decoder (Deep-DAC)”. In: *European radiology*, pp. 1–13.

Tai, YF and P Piccini (2004). “Applications of positron emission tomography (PET) in neurology”. In: *Journal of Neurology, Neurosurgery & Psychiatry* 75.5, pp. 669–676.

Tashima, Hideaki and Taiga Yamaya (2016). “Proposed helmet PET geometries with add-on detectors for high sensitivity brain imaging”. In: *Physics in Medicine & Biology* 61.19, p. 7205.

Vandenberghe, Stefaan et al. (2016). “Recent developments in time-of-flight PET”. In: *EJNMMI physics* 3.1, p. 3.

Vemuri, Prashanthi et al. (2017). “Tau-PET uptake: regional variation in average SUVR and impact of amyloid deposition”. In: *Alzheimer’s & Dementia: Diagnosis, Assessment & Disease Monitoring* 6, pp. 21–30.

Wadsak, W and M Mitterhauser (2010). “Basics and principles of radiopharmaceuticals for PET/CT”. In: *European journal of radiology* 73.3, pp. 461–469.

Wernick, Miles N and John N Aarsvold (2004). *Emission tomography: the fundamentals of PET and SPECT*. Elsevier.

Yang, Lucie, Dwaine Rieves, and Charles Ganley (2012). “Brain amyloid imaging—FDA approval of florbetapir F18 injection”. In: *New England Journal of Medicine* 367.10, pp. 885–887.

Yang, Xiaofeng et al. (2019). “MRI-based attenuation correction for brain PET/MRI based on anatomic signature and machine learning”. In: *Physics in Medicine & Biology* 64.2, p. 025001.

Zaidi, Habib (2001). “Scatter modelling and correction strategies in fully 3-D PET”. In: *Nuclear medicine communications* 22.11, pp. 1181–1184.

Zaidi, Habib and Bruce Hasegawa (2003). “Determination of the attenuation map in emission tomography”. In: *Journal of Nuclear Medicine* 44.2, pp. 291–315.

Zaidi, Habib and Kenneth F Koral (2004). “Scatter modelling and compensation in emission tomography”. In: *European journal of nuclear medicine and molecular imaging* 31.5, pp. 761–782.

Zaidi, Habib and Marie-Louise Montandon (2006). “The new challenges of brain PET imaging technology”. In: *Current Medical Imaging Reviews* 2.1, pp. 3–13.

Zaidi, Habib, Marie-Louise Montandon, and Steve Meikle (2007). “Strategies for attenuation compensation in neurological PET studies”. In: *Neuroimage* 34.2, pp. 518–541.

Zaidi, Habib et al. (2011). “Design and performance evaluation of a whole-body Ingenuity TF PET–MRI system”. In: *Physics in Medicine & Biology* 56.10, p. 3091.